Ionics (2023) 29:5183–5193
https://doi.org/10.1007/s11581-023-05212-7

RESEARCH

Facile synthesis of MoS_2/N-doped carbon as an anode for enhanced sodium-ion storage performance

Fang-Xiao Du[1] · Song-Li Liu[2] · Yang Li[2] · Jian-Kang Wang[2] · Peng Zhang[2]

Received: 19 July 2023 / Revised: 23 August 2023 / Accepted: 5 September 2023 / Published online: 26 September 2023

Abstract

The scalable synthesis of MoS_2/N-doped carbon (MoS_2/NC) nanosheets was accomplished using a facile salt template–assisted synthesis method. The MoS_2 nanosheets were uniformly encapsulated in nitrogen-doped carbon frameworks. As an anode for sodium-ion batteries (SIBs), the electrochemical performance of the MoS_2/NC electrode was significantly improved compared to pure MoS_2, which demonstrated a reversible capacity of 334.6 mAh g^{-1} after 100 cycles at 0.2 A g^{-1}; even after 250 cycles of 1 A g^{-1}, the capacity could still be maintained at 252.9 mAh g^{-1}. This excellent sodium storage performance was mainly due to the coupling of nitrogen-doped carbon with MoS_2 and the uniform distribution of the nanosheets, which improved the reaction kinetics. Besides, the electrochemical reconstruction ensured the integrity of the electrode. This work was of great significance for the large-scale synthesis of MoS_2 anode material with enhanced stability SIBs.

Keywords MoS_2/NC · Sodium-ion batteries · Anode material · Enhanced stability · Electrochemical reconstruction

Introduction

Lithium-ion batteries (LIBs), as an excellent energy storage material, have been developed rapidly in the past few decades [1]. However, the limited reserves cannot satisfy increasing demand [2]. By contrast, sodium element is abundant and low-cost. Besides this, compared with LIBs, sodium-ion batteries (SIBs) are safer and compatible with existing lithium-ion devices because of similar working principles, gradually becoming a research hotspot [3–5]. Unfortunately, the development of SIBs still has some limitations. For anode materials, traditional materials such as graphite are not enough to support the free penetration of sodium ions on account of the larger radius of Na. Some anode materials suitable for LIBs are insufficient for SIBs simultaneously [6, 7]. Therefore, it is one of the main tasks to design new anode materials appropriate for SIBs.

According to the sodium storage mechanism, SIB anode can be categorized into intercalation-, conversion-, and alloying-type materials. Transition metal oxides [8, 9] and sulfides [10, 11] show excellent electrochemical performance in various anode materials. Especially, MoS_2, with its unique layer-by-layer structure and high sodium-ion storage capacity, has tremendous development prospects in SIBs. Nevertheless, poor electrical conductivity and agglomeration tendency from the van der Waals force between MoS_2 layers lead to a long diffusion path and slow kinetics [12–14]. Furthermore, sodium-ion insertion/extraction repeatedly leads to significant volume expansion of MoS_2 and severe capacity decay in the cycle process, which results in poor cyclic capacity retention and rate capability [15–17].

To solve these intractable problems, a series of efforts such as doping [18, 19], multicomponent integration [20, 21], and morphology engineering [22, 23] have been made to improve the performance of MoS_2 for SIB anode. Among them, combining carbon with high conductivity is a very effective measure. The addition of carbon material can not only enhance the conductivity of MoS_2 but also buffer the volume variation during sodium insertion and extraction. For instance, Li et al. [24] grew MoS_2 nanosheets vertically on cotton-derived carbon fiber through hydrothermal and subsequent high-temperature carbonization processes. The material remained 323.1 mAh g^{-1} after 150 cycles at 0.5 A g^{-1}, showing good cycling performance. The predecessors introduced nitrogen doping on this basis to further improve

✉ Song-Li Liu
lsl@yznu.edu.cn

[1] College of Materials and Chemical Engineering, China Three Gorges University, Yichang 443002, China

[2] College of Materials Science and Engineering, Yangtze Normal University, Chongqing 408100, China

the cyclic properties of composites. N-doped carbon@MoS_2 nanosheet composite was obtained through the combination of hydrothermal synthesis and high-temperature annealing process using g-C_3N_4 as carbon and nitrogen source by Li et al. [25]. Owing to the great active sites for the storage of Na ion and enhancement of the diffusion rate and conductivity endowed by N-doped carbon, this material as an anode of SIBs had a profitable electrochemical capacity with a 246 mAh g^{-1} of high reversible capacity after 1000 cycles at 1.5 A g^{-1}. Although significant progress has been made, the synthesis methods are still relatively complex and unsuitable for large-scale synthesis. Hence, seeking a facile synthesis strategy with mild conditions and low cost to prepare MoS_2/NC nanosheets is still essential.

Herein, we synthesized MoS_2/NC nanosheets using a facile salt template–assisted synthesis method. The layered MoS_2 nanosheets were uniformly coated in nitrogen-doped carbon frameworks. As an anode for SIBs, the electrochemical performance of the electrode was significantly improved, such as high specific capacity and superior cycling behavior, due to the coupling of nitrogen-doped carbon with MoS_2 and electrochemical reconstruction, which provided improved electrical/ionic transporting capacity and architectural stability. This work provided a reference for studying and applying MoS_2 materials in SIBs.

Experimental section

Material

Ammonium molybdate ($(NH_4)_6Mo_7O_{24}{\cdot}4H_2O$), thiourea ($CS(NH_2)_2$), glucose ($C_6H_{12}O_6$), and sodium chloride (NaCl) were all analytical grade without extra purification requirement. All chemicals were purchased from Shanghai Aladdin Co., Ltd.

Preparation of MoS_2/NC

0.4 g $(NH_4)_6Mo_7O_{24}{\cdot}4H_2O$ and 0.4 g $CS(NH_2)_2$ were dispersed in 30 ml of deionized water, then 0.5 g $C_6H_{12}O_6$ and 0.5 g NaCl were added into the solution with stirring for 2 h to dissolve completely. The precursor was diverted to a porcelain boat and incinerated at 800℃ for 2 h in a protective atmosphere (Ar) with a heating rate of 5℃ per minute. The collected product was washed with distilled water and ethanol repeatedly after cooling to room temperature and then dried for 5 h in a vacuum oven at 60℃ to acquire the MoS_2/NC sample. As the control, the samples without adding NaCl (MoS_2/NC (no NaCl)) and pure MoS_2 were prepared in the same approach.

Electrochemical measurements

The coin-type battery was assembled according to the following process. Specifically, the active materials (70 wt%), acetylene black (20 wt%), and sodium alginate (10 wt%) were added to deionized water by thoroughly grinding to form a uniform slurry, and evenly spread on a Cu sheet, drying at 60℃ for 6 h to remove water, then copper foil was cut into discs a diameter of 14 mm, and subjected to vacuum drying for 12 h at 120℃. The mass loading of the electrode prepared was about 0.6–1.0 mg cm^{-2} and the amount of electrolyte in each battery was 40 µl. Using Na as the counter electrode and GF/D Whatman as the diaphragm, CR2032 coin batteries were fabricated in an expandable glove box for a series of tests. 1 M $NaClO_4$ was dissolved in ethylene carbonate/propylene carbonate (EC/PC, 1:1 vol %) and 5% fluoroethylene carbonate (FEC) was added as the electrolyte. The galvanostatic charge/discharge tests were carried out on the LAND Instrument (CT 3002A, Wuhan, China). The cyclic voltammograms (CV, 0.01–3 V, 0.2 mV s^{-1}) and electrical impedance diagrams (EIS, 100 kHz–0.01 Hz, 5 mV s^{-1}) of the samples were determined by an electrochemical workstation.

Material characterization

The crystalline structure and phase composition of the samples were analyzed by X-ray powder diffraction (XRD, Rigaku D/max-2500). The thermogravimetric analysis was carried out at a heating rise of 20 ℃ min^{-1} in the flowing air. The specific surface area and pore size distributions of the samples were obtained by analyzing the N_2 adsorption–desorption isotherms. The surface valence states of elements in the samples were characterized by X-ray photoelectron (XPS, Thermo Scientific ESCALAB XI^+) with monochromatic Al Kα as the X-ray source. The Raman spectra were obtained on the InVia reflex Raman spectroscope by using the laser excitation with a 532 nm. The microstructure was determined using a scanning electron microscope (SEM, Quanta FEG250) and a transmission electron microscope (TEM, Hitachi 800).

Results and discussion

The preparation process of MoS_2/NC nanosheets is shown in Fig. 1. First, the $(NH_4)_6Mo_7O_{24}{\cdot}4H_2O$, $CS(NH_2)_2$, $C_6H_{12}O_6$, and NaCl were dissolved in deionized water and stirred for several hours. Secondly, the mixture was dried to remove water so the MoS_2/NC precursor was well encased in the NaCl template. Subsequently, the obtained precursor was

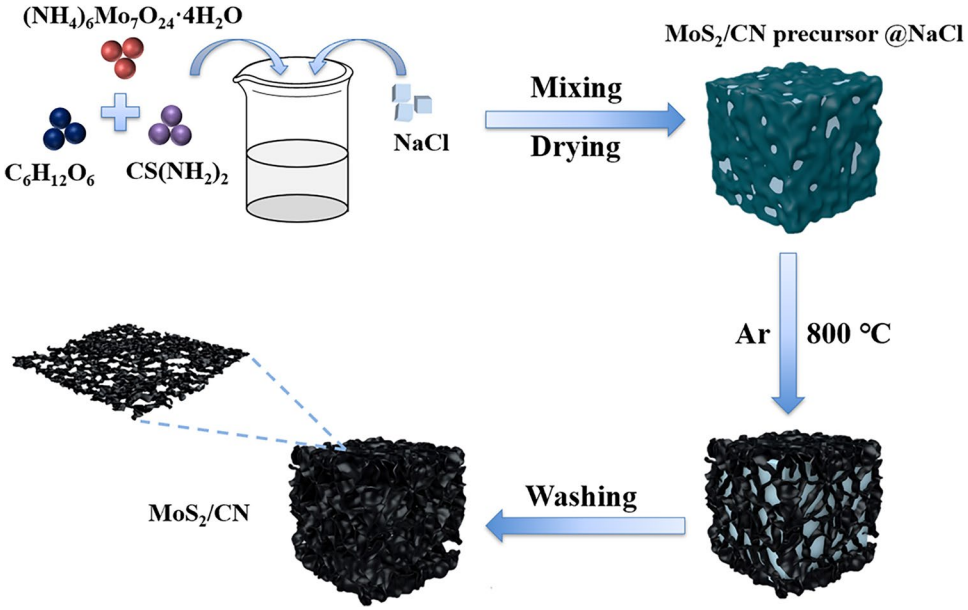

Fig. 1 Schematic illustration for the preparation of MoS_2/NC nanosheets by a one-pot calcination method

calcined in an Ar atmosphere. During the calcination process, Mo reacted with S ions, while glucose was carbonized at high temperatures and converted into an N-doped carbon framework. The interaction between the two made the MoS_2/NC nanosheets grow uniformly on the surface of the NaCl template surface. Finally, MoS_2/NC nanosheets were prepared by removing the NaCl template with deionized water.

XRD was conducted to characterize the crystalline of the pure MoS_2, MoS_2/NC (no NaCl), and MoS_2/NC. As shown in Fig. 2a, the diffraction peaks at 14.1°, 32.8°, 39.8°, 49.3°, and 58.7° corresponded to the (002), (100), (105), (103), and (110) planes of hexagonal MoS_2 crystal (JCPDS No. 37–1492), respectively. It was noteworthy that the peaks located at (002) of the MoS_2/NC and MoS_2/NC (no NaCl) were weak, which could be the presence of carbon inhibiting the growth of (002) lattice plane [26–28]. In addition, according to the Debye–Scherrer equation, the crystallite sizes of the pure MoS_2, MoS_2/NC (no NaCl), and MoS_2/NC samples were calculated using the peaks at (100) as 8.67 nm, 7.02 nm, and 7.08 nm, respectively. Compared with pure MoS_2, the XRD peaks of MoS_2/NC (no NaCl) and MoS_2/NC samples were broader and the calculated grain sizes were smaller, which might be caused by the reduction of crystallite size due to the addition of N-doped carbon [29]. Figure 2b presents the Raman spectra of the MoS_2/NC and the MoS_2 materials. Two peaks at 379 and 404 cm^{-1} were seen for the as-synthesized MoS_2 sample, representing the E^1_{2g} and A_{1g} vibration modes. Compared with pure MoS_2, apart from the characteristic peaks of MoS_2, the MoS_2/NC showed two broad peaks at 1354 cm^{-1} and 1578 cm^{-1}, which could be well indexed to the D (disordered carbon) and G (graphitic carbon) bands of carbon, respectively [30]. The former represented the sp^3 hybrid, and the latter was related to the sp^2 hybrid. The calculated value of I_D/I_G was 1.22, indicating that the obtained MoS_2/NC had a higher content of disordered carbon and more sp^3-bond carbon. Raman's results verified that pyrolyzed carbon and MoS_2 were successfully synthesized by this method. To estimate the relative contents of MoS_2 and C components in the MoS_2/NC sample, thermogravimetric (TG) analysis was carried out in an air atmosphere. The weight loss of the MoS_2 sample at 350 ℃–600 ℃was 9.86%, mainly because of the oxidation of pure MoS_2 into MoO_3 (Fig. S1) [31–33]. For the MoS_2/NC sample, the weight loss of the MoS_2/NC sample had

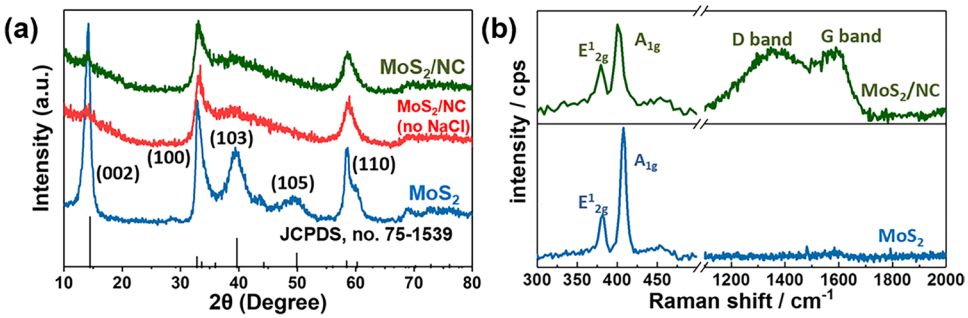

Fig. 2 **a** XRD patterns of MoS_2/NC, MoS_2/NC (no NaCl), and MoS_2. **b** Raman spectra of MoS_2/NC and MoS_2

increased to 35.9% at the same temperature range because of the oxidation of MoS_2 to MoO_3 and the combustion of carbon. Therefore, the contents of MoS_2 and carbon were 71.3% and 28.7%, respectively. Figure S2 shows the N_2 adsorption/desorption isotherms of MoS_2/NC and MoS_2 samples. The pure MoS_2 sample showed a typical IV isotherm with a H_3 hysteresis loop, while the MoS_2/NC sample displayed a H_2 hysteresis loop. The specific surface areas of the two samples calculated by the Brunauer–Emmett–Teller (BET) method were 5.95 $m^2\ g^{-1}$ and 4.73 $m^2\ g^{-1}$, respectively. The pore size distribution diagram showed that NaCl as a sacrificial template was crucial in reducing the pore size of the MoS_2/NC. Small pores could shorten diffusion pathways and facilitate sodium ions and electrons transfer during discharge and charge processes.

XPS was used to analyze the surface atomic composition of the samples of MoS_2/NC and MoS_2, as well as the results are displayed in Fig. 3. In the complete XPS spectra of the two samples, the signals of Mo, S, C, N, and O could be distinctly observed in MoS_2/NC sample, while the carbon content in pure MoS_2 sample was significantly reduced, which was consistent with the expected results (Fig. S3). Figure 3a depicts the high-resolution XPS spectrum in the 3d region of Mo, where the two peaks at 229.4 and 232.6 eV represented $3d_{5/2}$ and $3d_{3/2}$ of Mo^{4+}, respectively, and the peak at 226.7 eV corresponded to the 2s signal of S. A small peak could also be observed at 236 eV, which was the $3d_{3/2}$ signal of Mo^{6+} according to previous studies [34, 35]. The generation of this peak might resulted from the surface oxidation of the MoS_2/NC during the process of preparation and storage, which also explained the existence of the O element in the whole spectrum [36]. It can be seen from the XPS spectra of the S 2p region described in Fig. 3b that two peaks at 163.4 eV and 162.2 eV represented the $2p_{1/2}$ and $2p_{3/2}$ signals of S^{2-}, respectively. Similarly, a weak peak at 168.7 eV represented the S^{6+} signal, which was caused by the oxidation of S^{2-} in the atmosphere [37]. Compared with pure MoS_2, the peaks of Mo^{4+} 3d and S^{2-} 2p of the MoS_2/NC sample both shifted toward lower binding energy, which was caused by the increase of electron cloud density near MoS_2 due to the addition of C [38]. Figure 3c is the fitted XPS spectrum of the 1s region of C, where 284.6, 285.9, 287.0, and 288.8 eV were categorized as C–C, C-N/C-O, C-S, and C = O bonds, respectively. This result indicated that N elements were successfully doped into carbon, which was further corroborated by the N 1s spectrum in Fig. 3d. Three peaks at 398.3, 400.2, and 401.9 eV could be identified as the N 1s region, representing pyridinic N, pyrrolic N, and graphitic N, respectively. The addition of N could improve the electrochemical performance of the materials mainly from the following aspects: on the one hand, N had a high electronegativity, and N doping could enhance the interaction between particles, thereby improving the electrochemical activity of the material. On the other hand, N

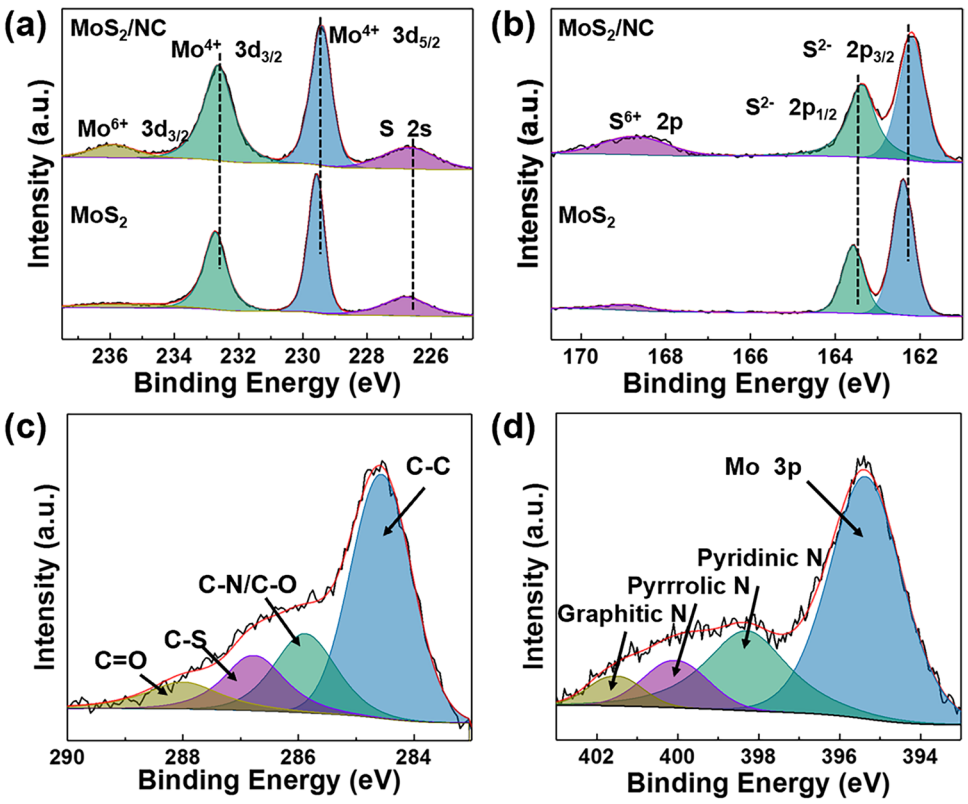

Fig. 3 XPS spectra of MoS_2/NC and MoS_2 **a** Mo 3d, **b** S 2p. XPS spectra of MoS_2/NC, **c** C 1s, **d** N 1s

doping could also provide more defects, which improved the transport rate of sodium ions by interacting with them [39, 40].

The morphological and microstructure characteristics were analyzed by SEM, TEM, and HRTEM. Figure 4a describes the SEM image of the MoS_2/NC (no NaCl) sample, and as shown in the figure, the single MoS_2/NC (no NaCl) sample presented an apparent massive structure. The MoS_2/NC exhibited a typical nanosheet structure that the MoS_2 nanosheets were uniformly embedded in the nitrogen-doped carbon frameworks (Fig. 4b, c). The results indicated that the addition of water-removable template NaCl could effectively restrain the aggregation of MoS_2 and promote nanosheet formation. The average layer spacing of about 0.626 nm was represented to the (002) plane of MoS_2 in the TEM and HRTEM images (Fig. 4d, e). Specifically, we could observe that the MoS_2 nanosheets composed of 3–4 layers were evenly dispersed in the carbon shell. The cross-linked structure of these nanosheets was small and well combined with the carbon layer. This unique structure could availably buffer the volume variation of MoS_2 during repeated charging-discharging processes, showing good cycling stability. The electron diffraction (SAED) pattern of the MoS_2/NC is shown in Fig. 1f, illustrating the polycrystalline nature of MoS_2. Figure 4g–k show the EDS mapping images of the MoS_2/NC. It was obvious that Mo, S, C, and N elements were uniformly distributed in the selected region. Based on the characterization mentioned above, the nanosheet-like MoS_2/N-doped carbon was successfully synthesized.

To investigate the electrochemical behavior of sodium storage in the sample MoS_2/NC, the electrode coated with 70% active substance was made into a button battery, and a series of electrochemical tests were carried out, such as the CV curves of MoS_2/NC cycling three times (Fig. 5a). During the first discharge, two strong peaks could be observed near 0.72 V and 0.36 V while one weak peak near 0.65 V and one strong peak at ca. 1.82 V were seen during the first anodic sweep. The reduction peak at 0.72V corresponded to the formation of Na_xMoS_2 by the reaction between Na^+ and MoS_2 (reaction 1). Another reduction peak at 0.36 V was caused by the conversion reaction of Na_xMoS_2 and Na^+ into Na_2S and Mo (reaction 2), accompanied by the formation of solid electrolyte interphase (SEI) film.

$$MoS_2 + xNa^+ + xe^- \rightarrow Na_xMoS_2 \quad (1)$$

$$Na_xMoS_2 + (4 - x)Na^+ + 4e^- \rightarrow Mo + 2Na_2S \quad (2)$$

The weak oxidation peak at 0.65 V was determined by the recombination of Na_2S with Mo into Na_xMoS_2, and the other oxidation peak at 1.82 V indicated the process of extracting

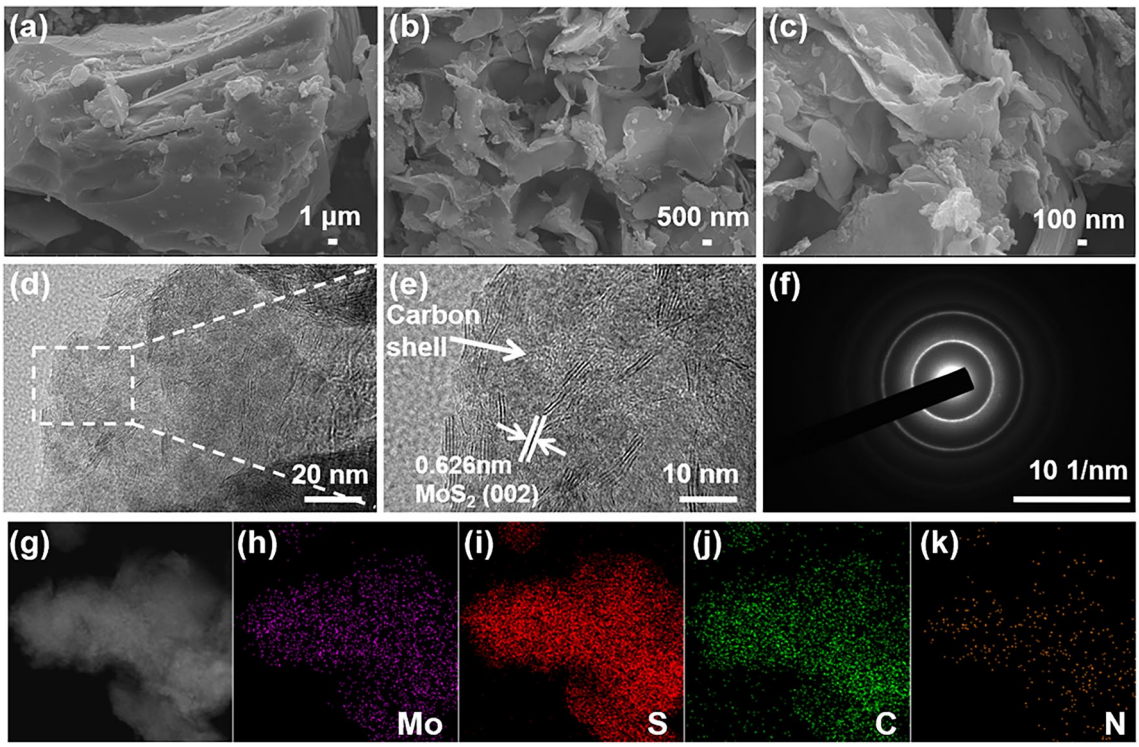

Fig. 4 SEM images of **a** MoS_2 (no NaCl), **b-c** MoS_2/CN. **d–e** HRTEM images of MoS_2/CN composite at different magnifications. **f** SAED patterns of MoS_2/CN. **g–k** EDS elemental mapping images of MoS_2/CN

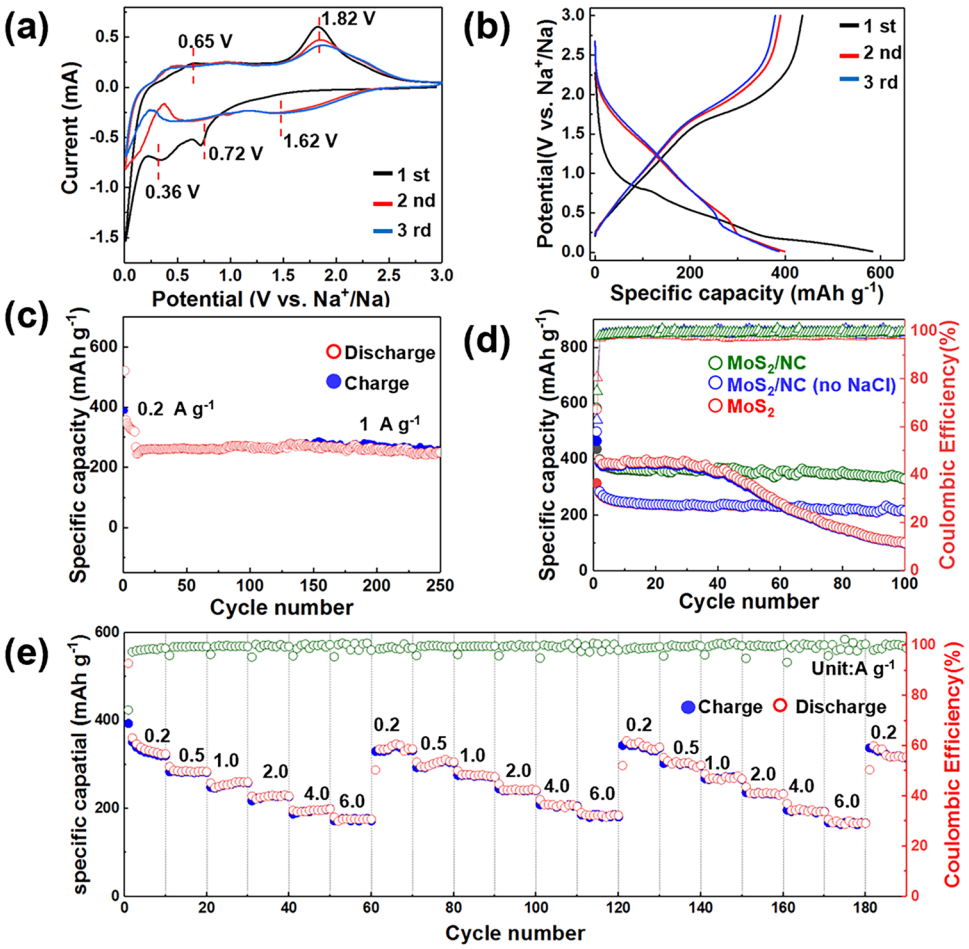

Fig. 5 **a** CV curves of MoS_2/NC electrode in the range of 0–3 V at a scanning rate of 0.2 mV s^{-1}. **b** Charge–discharge curves of different cycles at 0.2 A g^{-1}. **c** Cycling performance of MoS_2/NC, MoS_2/NC (no NaCl), and MoS_2 electrodes at 0.2 A g^{-1}. **d** Long-term cycling performance at 1 A g^{-1}. **e** Rate performance of MoS_2/NC electrode

Na^+ from Na_xMoS_2. At the end of the first cycle, the original MoS_2 was partly transformed into a small amount of amorphous S and elemental Mo. In the second cathodic sweep, a new reduction peak appeared at 1.62 V, corresponding to the conversion of amorphous S into Na_2S [41–44]. The reduction peak at 0.2–0.78 V remained unchanged but decreased intensity, indicating an irreversible phase transition occurred during the first cycle. In the subsequent few scans, the redox peaks overlapped highly, demonstrating that the MoS_2/NC electrode had outstanding cycle capacity retention.

Figure 5b represents the galvanostatic charge–discharge curves of the MoS_2/NC electrode at 0.2 A g^{-1} in different cycles. The electrode's potential dropped sharply above 1.0 V and slowly below 1.0 V during the first cycling process, as seen from the figure, which might be due to the presence of carbon [45]. During discharge, two voltage platforms could be seen at 0–0.25 V and 0.5–0.75 V, while during charge, a voltage platform occurs at 1.75–2.0 V, which were primarily in accordance with the peak value observed in the CV curve [46]. Besides, the initial discharging and charging specific capacities of MoS_2/NC electrode were 582.96 and 435.97 mAh g^{-1}, respectively, giving a Coulombic efficiency of 74.75%. Other irreversible reactions, such as electrolyte decomposition and SEI film formation, led to low initial Coulomb efficiency. The Coulomb efficiency of the electrode was above 98% in the subsequent cycles, indicating the formed SEI film was relatively stable [47–49]. Figure 5c describes the performance comparison of the electrodes of MoS_2/NC, MoS_2/NC (no NaCl) and MoS_2 for 100 cycles at 0.2 A g^{-1}. The reversible specific capacities of the three samples after 100 cycles were 334.6, 213.2, and 100.8 mAh g^{-1}, respectively, indicating that the specific capacity and cycling lifetime of MoS_2/NC electrode was higher than MoS_2/NC (no NaCl) and MoS_2. Additionally, the capacity of the single MoS_2 electrode decreased rapidly after 50 cycles, showing poor electrochemical stability, mainly because of the poor conductivity of the material and the great volume variation during sodium-ion intercalation/de-intercalation. Compared with pure MoS_2, the electrochemical performance of the MoS_2/NC electrode had been improved, mainly due to the following two aspects. On the one hand, the introduction of N-doped carbon and the uniform distribution of nanosheets could enhance the conductivity of the material, alleviate the volume change during the cycle, increase the specific surface area, which improved the reaction kinetics, and thus further optimize the specific capacity [50, 51]. On

the other hand, the electrochemical reconstruction phenomenon could enhance the architecture of the electrode, showing more excellent cyclic stability [52]. Figure 5d describes the long-term cycling capability of the MoS_2/NC electrode. The electrode could provide a reversible capacity of 252.9 mAh g^{-1} at 1 A g^{-1} after 250 cycles, demonstrating that the composite exhibits excellent long-term cycling behavior. Figure 5e describes the rate performance of the MoS_2/NC electrode. At 0.2, 0.5, 1.0, 2.0, 4.0, and 6.0 A g^{-1}, the reversible capacities were 351.3, 282.2, 258.6, 227.2, 199.67, and 172.31 mAh g^{-1}, respectively. The reversible capacity could quickly recover to 338.2 mAh g^{-1} after three large cycles when the current density returned to 0.2 A g^{-1}, indicating that the MoS_2/NC electrode had superior rate performance.

As one of the effective methods to study SIBs, electrochemical impedance spectroscopy has been conducted to investigate the electrochemical dynamics differences of MoS_2/NC and MoS_2 electrodes. The Nyquist plots were fitted from the equivalent circuit in Fig. 6a and b. In the equivalent circuit, R_1 was the internal resistance between electrode and electrolyte, CEP was the abbreviation of constant phase element, R_2 was charge transfer resistance, and Z_w was ascribed to the diffusion rate of sodium ions. As we all know, the Nyquist diagram consists of a semicircle and a diagonal line. The semicircle originated from the charge transfer resistance of the electrode, while the straight line was closely attributed to the impedance of the sodium-ion diffusion process. Table S1 lists the equivalent circuit parameters of different electrodes. The charge transfer resistance of the MoS_2/NC electrode was significantly lower than that of the MoS_2 electrode before cycling, showing faster reaction kinetics (Fig. 6a). After 50 cycles, the charge transfer resistance of the MoS_2/NC electrode was still less than that of MoS_2 (Fig. 6b). Due to the coupling of nitrogen-doped carbon with MoS_2 and the uniform distribution of the nanosheets making the electrolyte to be more easily permeated into the electrode, which improved the reaction kinetics, finally leading to a lower R_2 on the macroscale. In the low-frequency region, Fig. 6c and d show the Nyquist plots of the real part (Z′) of the two groups of samples versus $\omega^{-1/2}$. Among them, the Warburg coefficient was inversely proportional to the diffusion coefficient of sodium ions, which could be determined by the slope of the Z′ and $\omega^{-1/2}$ lines [53]. That was, the smaller the slope of the fitted line was, the larger the diffusion coefficient of sodium ion was, and the better the kinetic property of the electrode was. Calculated by fitting the slope of the curve, the diffusion coefficient of the MoS_2/NC electrode was 5.31×10^{-15} cm^2 s^{-1} after 50 cycles, which was higher than that of the pure MoS_2 electrode (7.29×10^{-18} cm^2 s^{-1}), indicating that MoS_2/NC could promote the transmission and diffusion of sodium ions, showing better electrochemical performance. The R_2 of both electrodes was decreased after 50 cycles, and compared with before cycling (2.19×10^{-15} cm^2 s^{-1}), the diffusion coefficient of the MoS_2/NC electrode after cycling was still higher (Fig. 6d), which was because of the crystal structure transformation of MoS_2 during cycling, which was consistent with those reported previously [54].

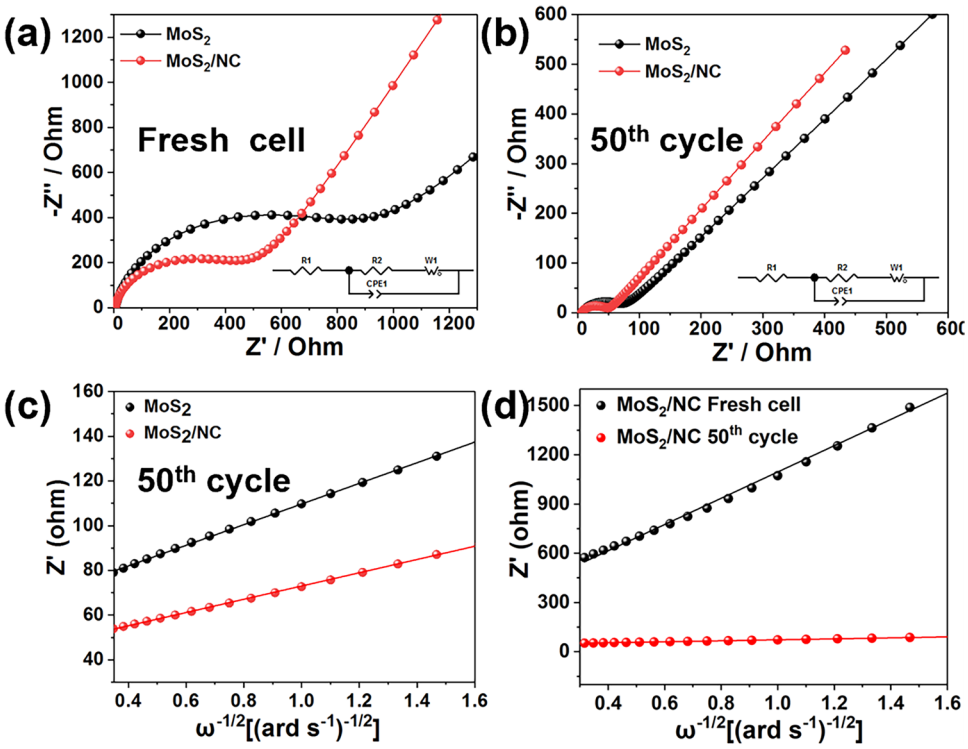

Fig. 6 Nyquist plots of the MoS_2 and MoS_2/NC electrodes **a** before cycling, **b** after 50 cycles. **c** The real parts of the MoS_2 and MoS_2/NC electrodes of the complex impedance versus $\omega^{-1/2}$ before cycling. **d** The real parts of the MoS_2/NC electrodes of the complex impedance versus $\omega^{-1/2}$ before cycling and after 50 cycles

To further investigate the cyclic kinetics of the MoS_2/NC electrode, CV tests were performed at the scanning rates of 0.2, 0.4, 0.6, 0.8, and 1.0 mV s^{-1}(Fig. 7a). These curves were similar in shape as could be seen from the figure, but with the increase in scanning rate, the values of peak currents increase. The capacitive process and diffusion behavior of the sodium storage mechanism could be qualitatively analyzed by the following Eqs. (3, 4):

$$i = av^b (0.5 \le b \le 1) \tag{3}$$

$$\log(i) = b \log(v) + \log(a) \tag{4}$$

where a and b were constants, i was identified as the current, and v represents the sweep speed. As we all know, the b value represented the type of reaction kinetics. When the b value approached 0.5, the reaction was mainly controlled by the diffusion behavior. When closer to 1, the storage of sodium ions was mainly dominated by the capacitive behavior [55, 56]. Linear fitting was performed on oxidation peaks 1, 2 and reduction peaks 3, 4 in Fig. 7b. b values of peaks 1, 2, 3, and 4 were 0.762, 0.936, 0.776, and 0.756, respectively. The results indicated that the sodium-ion storage kinetics of the MoS_2/NC composite was dominated by the capacitance behavior. According to the Eq. (5):

$$i = k_1 v + k_2 v^{1/2} \tag{5}$$

the capacitive contribution could be further calculated at different sweep rates, where $k_1 v$ corresponded capacitive process and $k_2 v^{1/2}$ represented the diffusion process. Figure 7c and d describe the calculated results. When the scanning rate was 0.2 mV s^{-1}, the contribution of the capacitive was 46.85%. It could be seen from the results that the contribution of capacitance improved with the increase in the sweep speed. When the scanning rate scaled up from 0.2 to 1.0 mV s^{-1}, the ratios were 46.9%, 50.6%, 62.4%, 63.0%, and 64.9%, respectively. For comparison, the CV curves of pure MoS_2 and MoS_2/NC (no NaCl) electrodes were measured at different scanning rates (Fig. S4). It was calculated that with the increase of scanning rate, the capacitance contributions of pure MoS_2 electrode were 48.7%, 52.9%, 55.1%, 57.2%, and 61.7%, respectively, and that of MoS_2/NC (no NaCl) electrode were 57.8%, 59.8% and 61.7%, 62.2%, and 64.6%, respectively. The capacitive contributions of MoS_2/NC (no NaCl) and MoS_2/NC electrodes were relatively higher than that of pure MoS_2 electrodes, indicating that N-doped carbon could improve the capacitive contribution and promote sodium-ion transfer.

To further study the reasons for the excellent electrochemical performance of the MoS_2/CN electrode, the morphological characteristics of the MoS_2/CN electrode were analyzed after 100 cycles at a specific current density. It could be seen that the size of the MoS_2 nanosheets in the electrode after cycling was reduced, and the irregular rectangular bulges were attached to the surface of the nanosheets (Fig. 8a). This morphology could also be observed in TEM, where the size of the rectangular bulges was about 60–80 nm as shown in Fig. 8b. Additionally, clear lattice fringes

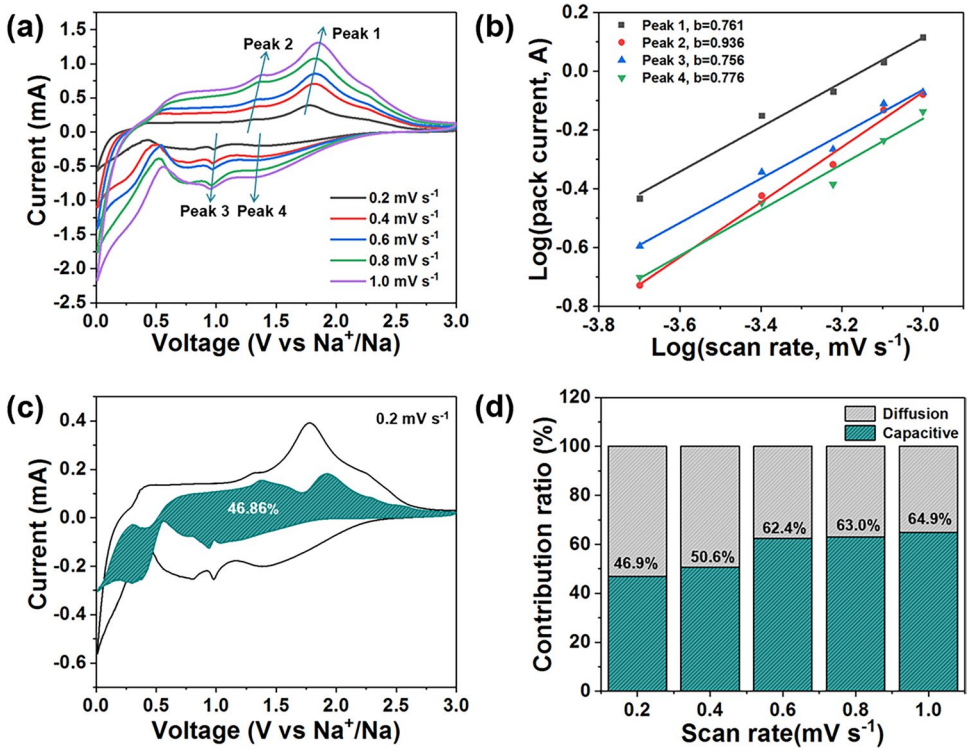

Fig. 7 **a** CV curves of MoS_2/CN electrode at different scanning rates. **b** The relationship between log (*i*) and log (*v*). **c** Capacitive contribution in the CV curve at a scan rate of 0.2 mV s^{-1} (shaded region). **d** Ratio of capacitive contributions at different scanning rates

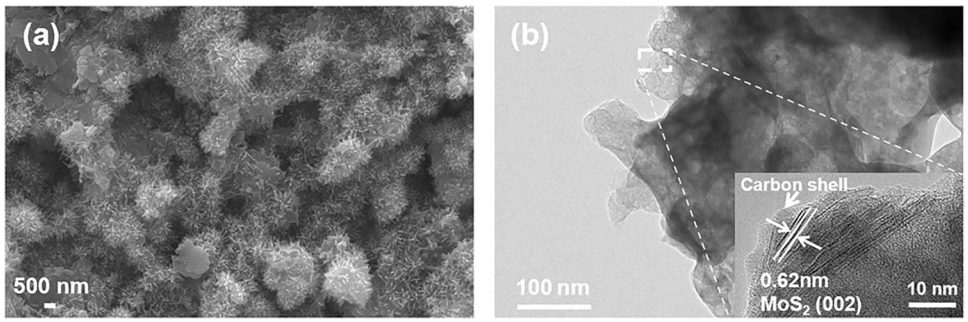

Fig. 8 **a** SEM, **b** HRTEM images of MoS_2/CN electrode after 100 cycles

could be observed on the HRTEM image, where the 0.62 nm interplanar spacing corresponded to the (002) face of MoS_2, which might be due to the electrochemical reconstruction phenomenon of the MoS_2/CN electrode during the cycle, that was, the reaction kinetics changed because of the evolution of the microstructure [54, 57]. With the reduction of the size of MoS_2 nanosheets and the formation of irregular rectangular bulges, the contact between the electrolyte and the electrode enhanced, thus exhibiting better electrochemical reaction kinetics, which was consistent with measurements of the EIS. This extraordinary morphological change might be the reason for the good stability of the MoS_2/CN electrode.

Conclusion

In summary, the MoS_2/CN nanosheets were prepared using a facile salt template–assisted synthesis method, in which the MoS_2 nanosheets were uniformly embedded in the nitrogen-doped carbon framework without severe agglomeration. The as-obtained MoS_2/NC nanosheets exhibited outstanding electrochemical properties (334.6 mA h g^{-1} at 0.2 A g^{-1} after 100 cycles), indicating that the MoS_2/CN nanosheets provided more excellent sodium storage properties, compared with pure MoS_2. The improved electrochemical performance could be caused by the coupling effect of N-doped carbon with MoS_2, which offered improved electrical/ionic transporting capability, and the electrochemical reconstruction, which guaranteed electrode stability. The electrode had the advantages of a simple synthesis method, low cost, and suitable for large-scale production, endowed MoS_2/NC potential prospect in energy conversion and storage.

Supplementary Information The online version contains supplementary material available at https://doi.org/10.1007/s11581-023-05212-7.

Author contribution Fang-Xiao Du performed the research and wrote the manuscript; Song-Li Liu, Yang Li, Jian-Kang Wang, and Peng Zhang all analyzed the data and were involved in the revision of the manuscript. All authors reviewed the manuscript.

Funding The work was supported by the Natural Science Foundation of Chongqing Science and Technology Bureau (Grant No. CSTB2022NSCQ-MSX0244 and cstc2022ycjh-bgzxm0037), the Science and Technology Research Program of Chongqing Municipal Education Commission (Grant No. KJZD-K202001402 and FLKJ,2022CBZ4059), and the Science and Technology Research Program of Chongqing Municipal Education Commission (Grant No. KJQN202101422).

Data availability The data presented in this paper are available on request from the corresponding author.

Declarations

Ethics approval This work did not include any studies involving humans or animals.

Competing interests The authors declare no competing interests.

References

1. Yang X, Rogach AL (2020) Anodes and sodium-free cathodes in sodium ion batteries. Adv Energy Mater 10(22):2000288. https://doi.org/10.1002/aenm.202000288
2. Yabuuchi N, Kubota K, Dahbi M et al (2014) Research development on sodium-ion batteries. Chem Rev 114(23):11636–11682. https://doi.org/10.1021/cr500192f
3. Liu Y, Wu X, Moeez A et al (2022) Na-rich $Na_3V_2(PO_4)_3$ cathodes for long cycling rechargeable sodium full cells. Adv Energy Mater 13(3):2203283. https://doi.org/10.1002/aenm.202203283
4. Feng W, Zhu L, Dong X et al (2022) Enhanced moisture stability of lithium-rich antiperovskites for sustainable all-solid-state lithium batteries. Adv Mater 25:636–643. https://doi.org/10.1002/adma.202210365
5. Wang Y, Qu Q, Li G et al (2016) 3D Interconnected and multiwalled carbon@MoS_2@carbon hollow nanocables as outstanding anodes for Na-ion batteries. Small 12(43):6033–6041. https://doi.org/10.1002/smll.201602268
6. Sun N, Guan Z, Liu Y et al (2019) Extended "adsorption–insertion" model: a new insight into the sodium storage mechanism of hard carbons. Adv Energy Mater 9(32):1901351. https://doi.org/10.1002/aenm.201901351
7. Cui J, Yao S, Kim J (2016) Recent progress in rational design of anode materials for high-performance Na-ion batteries. Energy Storage Mater 7:64–114. https://doi.org/10.1016/j.ensm.2016.12.005
8. Yang C, Xiang Q, Li X et al (2020) MoO_3 nanoplates: a high-capacity and long-life anode material for sodium-ion batteries.

Journal of Materials Scienc 55:12053–12064. https://doi.org/10.1007/s10853-020-04788-z
9. Li R, Qing L, Zhao W et al (2022) Co_3O_4/nitrogen-doped carbon nanoparticles for high-performance Li/Na-ion batteries. Ionics 28:2613–2622. https://doi.org/10.1007/s11581-021-04424-z
10. Xiao Y, Lee S, Sun Y (2016) The application of metal sulfides in sodium ion batteries. Adv Energy Mater 7(3):1601329. https://doi.org/10.1002/aenm.201601329
11. Yuan J, Qu B, Zhang Q et al (2020) Ion reservoir enabled by hierarchical bimetallic sulfides nanocages toward highly effective sodium storage. Small 16(31):1907261. https://doi.org/10.1002/smll.201907261
12. Wang H, Jiang H, Hu Y et al (2017) 2D MoS_2/polyaniline heterostructures with enlarged interlayer spacing for superior lithium and sodium storage. J Mater Chem A 5:5383–5389. https://doi.org/10.1039/C7TA00030H
13. Yang L, Wang S, Mao J et al (2012) Hierarchical MoS_2/polyaniline nanowires with excellent electrochemical performance for lithium-ion batteries. Adv Mater 25(8):1180–1184. https://doi.org/10.1002/adma.201203999
14. Hui Z, Hu L, Gong S et al (2021) Flower-petal-like Nb_2C MXene combined with MoS_2 as bifunctional catalysts towards enhanced lithium-sulfur batteries and hydrogen evolution. Electrochim Acta 404(1):139781. https://doi.org/10.1016/j.electacta.2021.139781
15. Wu J, Liu J, Cui J et al (2020) Dual-phase MoS_2 as a high-performance sodium-ion battery anode. J Mater Chem A 8:2114–2122. https://doi.org/10.1039/C9TA11913B
16. Zhou S, Liu S, Chen W et al (2021) A "biconcave-alleviated" strategy to construct Aspergillus niger-derived carbon/MoS_2 for ultrastable sodium ion storage. ACS Nan 15(8):13814–13825. https://doi.org/10.1021/acsnano.1c05590
17. Feng M, Zhang M, Zhang H et al (2019) Room-temperature carbon coating on MoS_2/graphene hybrids with carbon dioxide for enhanced sodium storage. Carbon 153:217–224. https://doi.org/10.1016/j.carbon.2019.07.021
18. Tao H, Li J, Li J et al (2021) Metallic phase $W_{0.9}Mo_{0.1}S_2$ for high-performance anode of sodium ion batteries through suppressing the dissolution of polysulfides. J Energy Chem 66:356–365. https://doi.org/10.1016/j.jechem.2021.08.026
19. Zhang R, Li H, Sun D et al (2018) Facile preparation of robust porous MoS_2/C nanosheet networks as anode material for sodium ion batteries. J Mater Sci 54:2472–2482. https://doi.org/10.1007/s10853-018-2991-z
20. Cui L, Tan C, Li Y et al (2021) Hierarchical Fe_2O_3@MoS_2/C nanorods as anode materials for sodium ion batteries with high cycle stability. ACS Appl Energy Mater 4(4):3757–3765. https://doi.org/10.1021/acsaem.1c00167
21. Xue F, Fan F, Zhu Z et al (2023) MoS_2/CoS heterostructures grown on carbon cloth as free-standing anodes for high-performance sodium-ion batteries. Nanoscale 15:6822–6829. https://doi.org/10.1039/D3NR00866E
22. Li J, Luo SH, Ding X et al (2018) NaCl-template assisted synthesis of 3D honeycomb-like $LiMnPO_4$/C with high rate and stable performance as lithium-ion battery cathodes. ACS Sustain Chem Eng 6(12):16683–16691. https://doi.org/10.1021/acssuschemeng.8b03935
23. Tang WJ, Wang XL, Xie D et al (2018) Hollow metallic 1T MoS_2 arrays grown on carbon cloth: a freestanding electrode for sodium ion batteries. J Mater Chem A 6:18318–18324. https://doi.org/10.1039/C8TA06905K
24. Li X, Yang Y, Liu J et al (2017) MoS_2/cotton-derived carbon fibers with enhanced cyclic performance for sodium-ion batteries. Appl Surf Sci 413:169–174. https://doi.org/10.1016/j.apsusc.2017.03.259
25. Li H, Yu G, Luo J et al (2022) Soft-template-assisted synthesis of petals-like MoS_2 nanosheets covered with N-doped carbon for long cycle-life sodium-ion battery anode. J Electroanal Chem 922:116715. https://doi.org/10.1016/j.jelechem.2022.116715
26. Li J, Gao W, Huang L et al (2021) In situ formation of few-layered MoS_2@N-doped carbon network as high performance anode materials for sodium-ion batteries. Appl Surf Sci 571:151307. https://doi.org/10.1016/j.apsusc.2021.151307
27. Liu G, Cui J, Luo R et al (2019) 2D MoS_2 grown on biomass-based hollow carbon fibers for energy storage. Appl Surf Sci 469:854–863. https://doi.org/10.1016/j.apsusc.2018.11.067
28. Sun D, Ye D, Liu P et al (2017) MoS_2/graphene nanosheets from commercial bulky MoS_2 and graphite as anode materials for high rate sodium-ion batteries. Adv Energy Mater 8(10):1702383. https://doi.org/10.1002/aenm.201702383
29. Kandula S, Shrestha KR, Kim NH et al (2018) Fabrication of a 3D hierarchical sandwich Co_9S_8/α-MnS@N-C@MoS_2 nanowire architectures as advanced electrode material for high performance hybrid supercapacitors. Small 14(23):1800291. https://doi.org/10.1002/smll.201800291
30. Guruprasad K, Maiyalagan T, Shanmugam S (2019) Phosphorus doped MoS_2 nanosheet promoted with nitrogen, sulfur dual doped reduced graphene oxide as an effective electrocatalyst for hydrogen evolution reaction. ACS Appl Energy Mater 2(9):6184–6194. https://doi.org/10.1021/acsaem.9b00629
31. Wang Z, Chen T, Chen W et al (2012) CTAB-assisted synthesis of single-layer MoS_2-graphene composites as anode materials of Li-ion batteries. J Mater Chem A 1(6):2202–2210. https://doi.org/10.1039/C2TA00598K
32. Shan TT, Xin S, You Y et al (2016) Combining nitrogen-doped graphene sheets and MoS_2: a unique film-foam-film structure for enhanced lithium storage. Angew Chem Int Ed 55(41):12783–12788. https://doi.org/10.1002/anie.201606870
33. Sun W, Hu Z, Wang C et al (2016) Effects of carbon content on the electrochemical performances of MoS_2-C nanocomposites for Li-ion batteries. ACS Appl Mater Interfaces 8(34):22168–22174. https://doi.org/10.1021/acsami.6b05594
34. Yuan Z, Wang L, Li D et al (2021) Carbon-reinforced Nb_2CTx MXene/MoS_2 nanosheets as a superior rate and high-capacity anode for sodium-ion batteries. ACS Nano 15(4):7439–7450. https://doi.org/10.1021/acsnano.1c00849
35. Mei Y, Li TT, Qing J et al (2020) Construction of a C@MoS_2@C sandwiched heterostructure for accelerating the pH-universal hydrogen evolution reaction. Chem Commun 56:13393–13396. https://doi.org/10.1039/D0CC06049F
36. Jeong SY, Park SK, Kang YC et al (2018) One-dimensional nanostructure comprising $MoSe_2$ nanosheets and carbon with uniformly defined nanovoids as an anode for high-performance sodium-ion batteries. Chem Eng J 56:13393–13396. https://doi.org/10.1016/j.cej.2018.06.130
37. Qiu H, Zheng H, Jin Y et al (2020) Dopamine-derived N-doped carbon-encapsulated MoS_2 microspheres as a high-performance anode for sodium-ion batteries. Ionics 26:5543–5551. https://doi.org/10.1007/s11581-020-03734-y
38. Pan Q, Zhang Q, Zhang F et al (2018) Construction of MoS_2/C hierarchical tubular heterostructures for high-performance sodium ion batteries. ACS Nano 12(12):12578–12586. https://doi.org/10.1021/acsnano.8b07172
39. Wu J, Pan Z, Zhang Y et al (2018) The recent progress of nitrogen-doped carbon nanomaterials for electrochemical batteries. J Mater Chem A 6(27):12932–12944. https://doi.org/10.1039/C8TA03968B
40. Maulana AY, Song J, Futalan CM et al (2022) Improved reversibility of phase transformations using electron-rich graphitic carbon matrix in FeF_2 cathode for sodium-ion batteries. Chem Eng J 434:134727. https://doi.org/10.1016/j.cej.2022.134727
41. Chen B, Lu H, Zhou J et al (2018) Porous MoS_2/carbon spheres anchored on 3D interconnected multiwall carbon

nanotube networks for ultrafast Na storage. Adv Energy Mater 8(15):1702909. https://doi.org/10.1002/aenm.201702909
42. Hai S, Shen X, Ting M et al (2017) Reversible conversion of MoS_2 upon sodium extraction. Nano Energy 41:217–224. https://doi.org/10.1016/j.nanoen.2017.09.039
43. Liu P, Cai S, Zuo Y et al (2021) Synthesis of interlayer expanded MoS_2 by sulfurization of MoO_3 with enhanced sodium-ion storage. J Alloys Compds 895:162691. https://doi.org/10.1016/j.jallcom.2021.162691
44. Zhang X, Shi H, Liu L et al (2021) Construction of MoS_2/Mxene heterostructure on stress-modulated kapok fiber for high-rate sodium-ion batteries. J Colloid Interface Sci 605:472–482. https://doi.org/10.1016/j.jcis.2021.07.097
45. Li J, Ding Z, Pan L et al (2021) Facile self-templating synthesis of layered carbon with N, S dual doping for highly efficient sodium storage. Carbon 173:31–40. https://doi.org/10.1016/j.carbon.2020.10.092
46. Li J, Ding Z, Li J et al (2020) Synergistic coupling of $NiS_{1.03}$ nanoparticle with S-doped reduced graphene oxide for enhanced lithium and sodium storage. Chem Eng J 407:127199. https://doi.org/10.1016/j.cej.2020.127199
47. Yuan Z, Cao J, Valerii S et al (2021) MXene-Bonded hollow MoS_2/carbon sphere strategy for high-performance flexible sodium ion storage. Chem Eng J 430:132755. https://doi.org/10.1016/j.cej.2021.132755
48. Jing L, Lian G, Niu F et al (2018) Few-atomic-layered hollow nanospheres constructed from alternate intercalation of carbon and MoS_2 monolayers for sodium and lithium storage. Nano Energy 51:546–555. https://doi.org/10.1016/j.nanoen.2018.06.084
49. Ge M, Rong J, Fang X et al (2012) Porous doped silicon nanowires for lithium ion battery anode with long cycle life. Nano Lett 12(5):2318–2323. https://doi.org/10.1021/nl300206e
50. Wu C, Ou JZ, He F et al (2019) Three-dimensional MoS_2/carbon sandwiched architecture for boosted lithium storage capability. Nano Energy 65:104061. https://doi.org/10.1016/j.nanoen.2019.104061
51. Lu Y, Zhao Q, Zhang N et al (2015) Facile spraying synthesis and high-performance sodium storage of mesoporous MoS_2/C microspheres. Adv Func Mater 26(6):911–918. https://doi.org/10.1002/adfm.201504062
52. Hu X, Chen J, Zeng G et al (2017) Robust 3D macroporous structures with SnS nanoparticles decorating nitrogen-doped carbon nanosheet networks for high performance sodium-ion batteries. J Mater Chem A 5(45):23460–23470. https://doi.org/10.1039/C7TA08169C
53. Li Y, Kong LB, Liu MC et al (2017) Facile synthesis of $Co_3V_2O_8$ nanoparticle arrays on Ni foam as binder-free electrode with improved lithium storage properties. Ceram Int 43(1):1166–1173. https://doi.org/10.1039/C7TA02616A
54. Cho JS, Park JS, Jeon KM et al (2017) 1-D nanostructure comprising porous $Fe2O_3$/Se composite nanorods with numerous nanovoids, and their electrochemical properties for use in lithium-ion batteries. J Mater Chem A 5(21):10632–10639. https://doi.org/10.1039/C7TA02616A
55. Chen Z, Wu R, Liu M et al (2017) General synthesis of dual carbon-confined metal sulfides quantum dots toward high-performance anodes for sodium-ion batteries. Adv Funct Mater 27(38):1702046. https://doi.org/10.1002/adfm.201702046
56. Tu F, Han Y, Du Y et al (2018) Hierarchical nanospheres constructed by ultrathin MoS2 nanosheets braced on nitrogen-doped carbon polyhedra for efficient lithium and sodium storage. ACS Appl Mater Interfaces 11(2):2112–2119. https://doi.org/10.1021/acsami.8b19662
57. Bai X, Li D, Zhang D et al (2023) Boosting high-rate lithium storage in Li_3VO_4 via a honeycomb structure design and electrochemical reconstruction. J Mater Chem A 11(23):12164–12175. https://doi.org/10.1039/D3TA01817B